CRYSTAL GROWTH OF $KTa_{1-x}Nb_xO_3$ $(0 < x \leqslant 0.04)$ SOLID SOLUTIONS BY A SLOW-COOLING METHOD

D. RYTZ *

Institut de Physique Expérimentale, Swiss Federal Institute of Technology, CH-1015 Lausanne, Switzerland

and

H.J. SCHEEL

IBM Zurich Research Laboratory, CH-8803 Rüschlikon, Switzerland

For ferroelectric quantum-limit investigations, $KTa_{1-x}Nb_xO_3$ solid solutions with low Nb concentrations are of current interest. Large crystals ($25 \times 25 \times 12$ mm³) have been grown by a slow-cooling method using the accelerated crucible rotation technique ACRT. The experiments are described in some detail, and the experimental parameters related to the various types of inhomogeneity observed in such solid solutions. Moreover, the concentration gradient and the striations have been investigated by acoustic resonance and electron-microprobe measurements. Very faint striations may still exist in the crystals obtained as indicated by weak strain patterns in polarized light. These striations have been minimized in the ACRT experiments.

1. Introduction

The interest in high-quality $KTa_{1-x}Nb_xO_3$ crystals originates from the very large electro-optic effects [1] found in this material at temperatures just above the ferroelectric Curie point. For room-temperature applications, the optimum electro-optic properties are obtained in crystals with $T_c \approx 10°C$, i.e. $KTa_{0.65}Nb_{0.35}O_3$ often abbreviated as "KTN". Many attempts have been made to grow KTN crystals of sufficient size and perfection (these are listed in table 2 and will be briefly discussed in section 3). To our knowledge, large striation-free mixed crystals could not be grown reproducibly, so that other "pure" materials with smaller electro-optic effects ($LiNbO_3$ and KH_2PO_4, for example) are used for technological applications. However, basic research in the field of phase transitions has rediscovered the $KTa_{1-x}Nb_xO_3$ system. When working with small concentrations ($x \leqslant 0.02$), the Curie point may be adjusted in a temperature range ($T_c \leqslant 30$ K), where quantum effects become easily observable [2]. This system has become a prototype for such studies as outlined in section 2.

The present work describes the growth of $KTa_{1-x}Nb_xO_3$ crystals within a composition range $0 < x \leqslant 0.04$ for investigations at the ferroelectric quantum limit. The slow-cooling method has been chosen [3a] because of its relative simplicity and the technology available in combination with the *accelerated crucible rotation technique*, ACRT [4]. In section 3, the experimental conditions (mass of melt and cooling interval) are analysed theoretically and related to crystal size and homogeneity for samples in the above-mentioned composition range. Obviously, slow cooling leads to an inherent bulk concentration gradient in the case of solid solutions. In section 4, both theoretical and experimental evidence for this concentration gradient

Table 1
Physical properties of $KTaO_3$, $KNbO_3$ and $KTa_{1-x}Nb_xO_3$

	$KTaO_3$	$KTa_{1-x}Nb_xO_3$		$KNbO_3$	Refs.
Melting point T_M (°C)	1357			1039	[5]
	1372			1064	[6]
Density ρ (g cm^{-3})	6.97	$0 \leqslant x \leqslant 1$	$6.97 - 2.38x$	4.59	[7]
Hardness (mohs)	7				[8]
Refraction index n (cubic structure) at 546 nm	2.27	$x = 0.35$	2.34		[1,8]
Lattice constant $V^{1/3}$ (Å)					
at 20°C	3.9885 (cubic)	$x = 0.37$	3.9941 (cubic)	4.016 (orthorhombic)	[9–15]
		$x = 0.44$	3.997 (tetragonal)	4.0188 (orthorhombic)	
at 450°C	3.9924 (cubic)			4.024 (cubic)	
Thermal expansion $(a^{-1}) \Delta a / \Delta T$ (K^{-1})	2.6×10^{-6} ($0 < T < 300$ K)	$x = 0.37$	5.6×10^{-6} ($25 < T < 46$°C)		[9–15]
	6.8×10^{-6} ($T > 300$ K)				
Elastic compliances ((T Pa)$^{-1}$)	$s_{11} = 2.70$ (300 K)			$s_{11} = 4.62$ (733 K)	[16–18]
	$s_{44} = 9.2$			$s_{44} = 11.1$	
	$s_{12} = -0.63$			$s_{12} = -1.10$	
Ferroelectric transition temperature T_c (K)	None	$x = 0.35$	283	708	[19]

will be given. The crystal-growth experiments and results are described in section 5 and compared with earlier work. In sections 6 and 7, characterization results are described including microprobe analysis, optical microscopy, dielectric and acoustic measurements. Special emphasis is laid onto striations and their relation to the experimental growth parameters such as temperature control and ACRT.

2. The system KTaO$_3$–KNbO$_3$

KTaO$_3$ and KNbO$_3$, and their continuous series of solid solutions KTa$_{1-x}$Nb$_x$O$_3$ [5,6], are of perovskite ABO$_3$ type with the B site at the centre of the oxygen octahedra occupied by either Ta^{5+} or Nb^{5+} ions. Some of the properties of the end members KTaO$_3$ ($x = 0$) and KNbO$_3$ ($x = 1$) are listed in table 1, and references are quoted for KTa$_{1-x}$Nb$_x$O$_3$ with intermediate concentration x [7–19]. An essential feature of the KTa$_{1-x}$Nb$_x$O$_3$ crystals is that the paraelectric-to-ferroelectric transition temperature T_c can be adjusted by varying the composition [19] as illustrated in fig. 1. The sequence of structural transitions from cubic to rhombohedral can be observed down to $x = 0.05$ [19–22]. Note that there is a change in the order of the paraelectric-to-ferroelectric transition: below $x = 0.30$, the transition is of second order, whereas it is of first order for $x > 0.30$ [20,23].

For low concentrations and thus for very low Curie temperatures ($T_c \leqslant 50$ K), only a single transition is observed [22] and the function T_c versus x deviates strongly from the linear dependence observed for $x \geqslant 0.05$ (i.e. T_c varies as $\sqrt{x - x_c}$ for $x \leqslant 0.05$). At the critical concentration $x_c = 0.008$, the transition vanishes. For $x < x_c$, the paraelectric phase is stable down to absolute zero. The concentration x_c determines the so-called *quantum limit*, where quantum-mechanical zero-point energy fluctuations hinder the ferroelectric phase transition [25,26]. In this quantum regime, the critical properties are strongly modified [27].

3. Relation of crystal homogeneity and size to experimental parameters

In the growth of solid solutions, temperature changes obviously produce composition changes. From the phase diagram of KTaO$_3$–KNbO$_3$ [5],
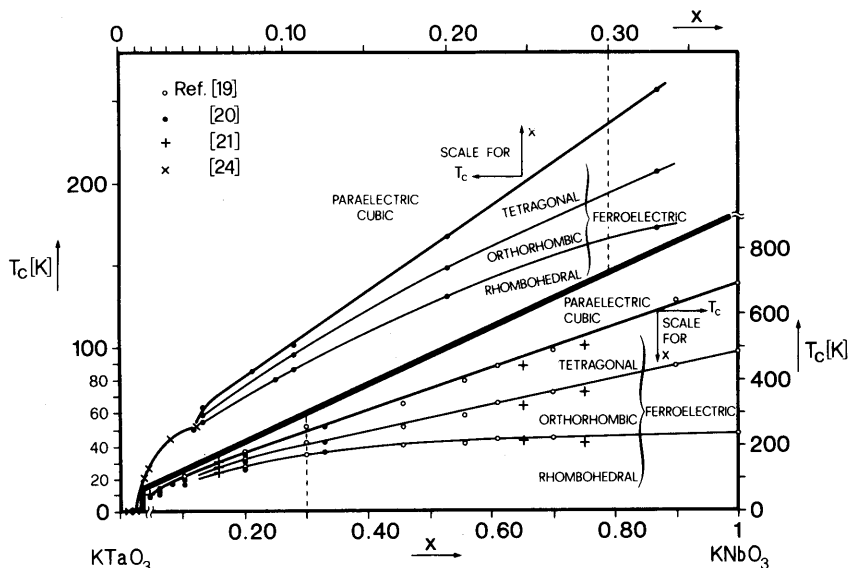

Fig. 1. Concentration dependence of the paraelectric cubic–ferroelectric tetragonal (thick solid curves) and tetragonal-orthorhombic–rhombohedral (thin solid curves) transition temperatures. Note the two different scales for $0 \leqslant x \leqslant 0.30$ and $0.05 \leqslant x \leqslant 1.00$. The dashed line indicates the concentration where the order of the paraelectric–ferroelectric transition changes: below $x = 0.30$ the transition is of second order, whereas it is of first order for $x > 0.30$.
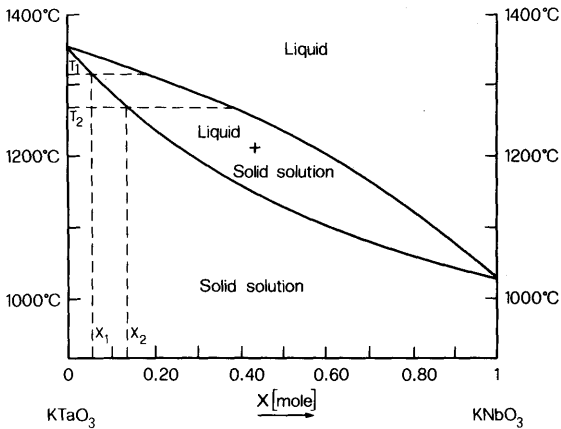
Fig. 2. Schematic solid-solution phase diagram (after ref. [5]). Growth starts at temperature T_1 with an initial concentration x_1, and ends at temperature T_2 with a final concentration x_2.

Fig. 3. Plot of crystal size V and inhomogeneity $x_1 - x_2$ as a function of experimental parameters (mass of melt M and cooling interval $T_1 - T_2$). A numerical example is detailed in the text.

one can evaluate the inhomogeneity $x_1 - x_2$ of one crystal growing in the temperature interval from T_1 to T_2 (fig. 2). The volume of crystal of density ρ growing from the total mass of the melt M is

$$V\,[\text{cm}^3] = 5.5 \times 10^{-4} \frac{M\,[\text{g}]}{\rho\,[\text{g cm}^{-3}]}$$
$$\times (T_1 - T_2)\,[°\text{C}], \qquad (1)$$

and its inhomogeneity

$$x_1 - x_2\,[\text{mol}] = \frac{T_1 - T_2\,[°\text{C}]}{600}. \qquad (2)$$

The relations (1) and (2) are valid near equilibrium conditions (i.e. for small cooling rates) for the $0 < x \leq 0.04$ range of the phase diagram. For other x values, the numerical prefactors have to be adjusted.

Fig. 3 is a nomogram of the relationship between the volume V and the inhomogeneity $x_1 - x_2$ of one crystal according to eqs. (1) and (2). This nomogram has been applied to predict the size and inhomogeneity of a crystal grown at given experimental conditions $(M, T_1 - T_2)$: For example, with $M = 1000$ g (requiring a platinum crucible of 300 to 500 ml) and $T_1 - T_2 = 20°$C, one obtains $V = 1.6$ cm^3 and $\Delta x = 0.033$. To achieve homogeneous crystals, large melt masses and small cooling intervals [19,28] are favourable. The first condition
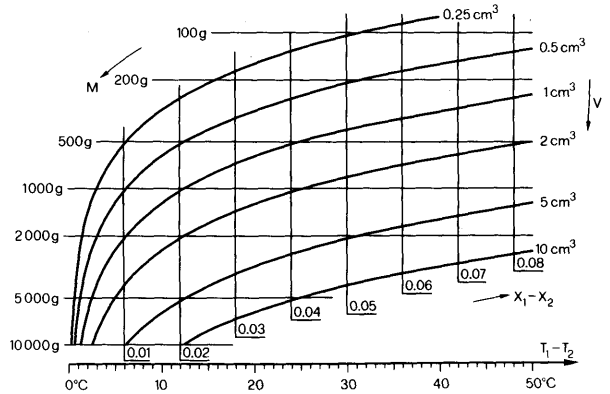
necessitates large crucibles and large amounts of high-purity chemicals, whereas for desirable small temperature intervals, the uncertainty of the nucleation temperature sets a practical limit. Obviously, this concept also applies to top-seeded solution growth (TSSG) with slow cooling and/or crystal cooling, but not to transport techniques.

Let us now consider the various experiments reported in the literature (see table 2 and refs. [19,20,22,24,28–46]). When comparing these experiments, it should be borne in mind that the calculated inhomogeneity of the entire volume of the as-grown crystal overestimates the measured inhomogeneity of a probe. The measured Δx values, therefore, can be smaller than the calculated $x_1 - x_2$ values. Additionally, it should be noted that it is only two times "easier" to achieve a given small inhomogeneity in the low-concentration $0 < x \leq 0.04$ range than in the technological $x \approx 0.35$ case (this factor of two is determined by comparing the corresponding slopes of the solidus curve in the phase diagram for the same precision of temperature control).

4. Inherent concentration gradients

Not only the concentration but also the concentration gradient in a solid-solution crystal varies

Table 2
Characteristics of various growth experiments of $KTa_{1-x}Nb_xO_3$ mixed crystals

Refs.	Composition range	Growth method	Thermal regulation	Cooling interval	Cooling rate ($°C\ h^{-1}$)	Mass of melt (g)	Composition of melt (mole% K_2CO_3)	Additives	Loss ($g\ h^{-1}$)
[19]	$0.2 \leqslant x \leqslant 1.0$	Kyropoulos	$\pm 0.1°C$	$\sim 15°C$	0.1–0.5	20	50	None	?
[29]	0.35	TSSG	?	?	0.1	1300	50–52	SnO_2 (0.1 mole%)	?
[30]	0.35	TSSG and "floating crystal"	?	?	?	350	53–60	None	0.06–0.2
[31]	0.35	Hydrothermal	?	–	–	–	Excess KOH		–
[32]	0.35	TSSG	?	?	?	32000	50	CaO, PbO,...	0.2
[33]	0.35	Hydrothermal	?	–	–	10	Excess KOH	SnO_2 (1 wt%)	–
[34]	$0.30 \leqslant x \leqslant 0.39$	Pfann technique	$\pm 0.5°C$	–	–	1400	65	SnO_2 (0.5 wt%)	?
[35]	$0.40 \leqslant x \leqslant 0.55$	TSSG and spontaneous nucl.	?	?	2–6	600	70	None	?
[36]	$0.34 \leqslant x \leqslant 0.40$	TSSG	?	?	?	1000	52–65	SnO_2 (0.1 mole%)	?
[37]	0.25	TSSG	?	?	?	800	52	None	?
[20, see also ref. [8]	$0.05 \leqslant x \leqslant 0.60$	TSSG	?	?	0.5	?	60	SnO_2 (10 ppm)	?
[38], see also ref. [39]	Various	TSSG	?	?	?	800	$\geqslant 50$		?
[28]	0.38	Mass transfer	$\pm 0.1°C$	–	–	400	55	None	?
[40]	0.35	Mass transfer	?	–	–	1400	53.5	SnO_2 (0.1 mole%)	?
[41]	0.35	Mass transfer	$\pm 0.1°C$	–	–	400	55	None	Considerable
[22], see also refs. [24,42–44]	$0 \leqslant x \leqslant 0.10$	Spontaneous nucl.	$\pm 2°C$	$500°C$	5	20	55–60	CuO, Fe_2O_3,...	?
[45]	0.28 and 0.40	Mass transfer	?	–	–	?		None	?
[46]	0.30	TSSG	?	?	?	?	?		?
Present work	$0 < x < 0.04$	Slow cooling	$\pm 0.1°C$	$\sim 40°C$	0.15	1100	60	None	0.1

Table 2 (continued)

| Refs.	Growth rate ($\mathring{A} \, s^{-1}$)	Size of resulting crystals (mm^3)	Developed faces	Colour	Characterization	Measured Δx (local)	Calculated Δx (total)	Striations	Other defects
[19]	350	6.5×6.5×3.2	(100)		Dielectric constant	0.03	0.10	?	
[29]	720	15×10×10	(100)	Colourless	Dielectric constant	0.002	0.02	Yes	
[30]	2800	15×∅ 10		Colourless	X-ray fluorescence	?	0.06	Yes	"Some" strain
[31]	?			Colourless	X-rays; microprobe	?	–	Yes	Exsolution patterns
[32]	360	80×80×30	(100) and minor (110)	Colourless	X-ray fluorescence	0.01	0.10	Yes	
[33]	710	5×5×5	(100) and minor (111)			?	–	Yes	
[34]	850	40×40×30	(100)		Dielectric constant	0.01	–	Yes	
[35]	?	8×∅ 15 5×5×2		Pale yellow	X-rays; dielectric constant	?	0.04	?	Cracks
[36]	?	?		Colourless	Resistivity	?	?	?	
[37]	2000	8×8×7	(100)		Dielectric constant	0.01	0.01	?	
[20], see also ref. [8]	1400	1000–3000	(100)		Volumetric method	0.08	?	?	Large strain; grain boundaries
[38], see also ref. [39]	400–2800	2000	(100)			0.01	0.04	?	Mosaic spread 0.02°
[28]	220–420	1000	(100) and minor (110)	Colourless	Resistivity	?	–	?	
[40]	4000	50×50×10	(100)	Colourless		?	–	Yes	Inclusions
[41]	1200	30×30×20	(100) and minor (110)		Microprobe	0.04	–	Yes	
[22], see also refs. [24,42–44]	300	10×5×5	(100)	Yellow	Microprobe; density; dielectric constant; elastic step	0.003	0.25	Yes	
[45]	120	1000		Colourless	Dielectric constant; resistivity	?	–	?	Mosaic spread 0.01°
[46]	?	?		Blue	Resistivity	?	?	?	
Present work	100–400	25×25×10	(100)	Colourless	Microprobe; elastic step	<0.03	0.06	Very faint	
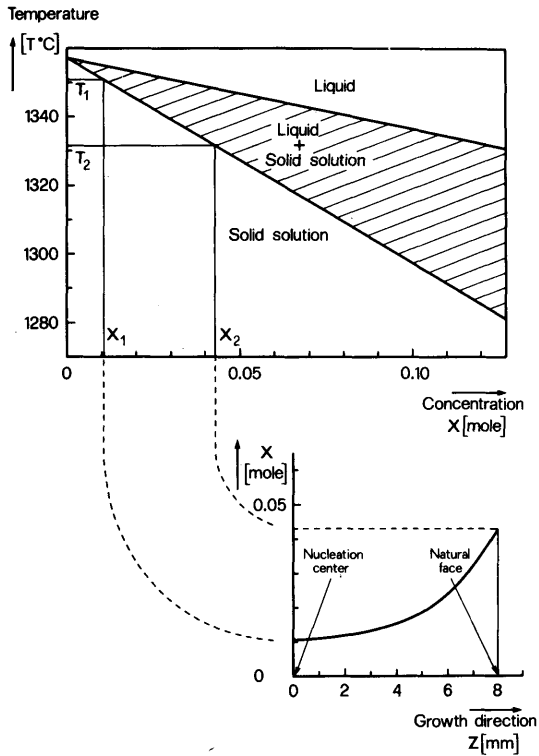
Fig. 4. Schematic phase diagram of KTa$_{1-x}$Nb$_x$O$_3$ and spatial variation of the concentration x along the growth direction z. The inherent bulk concentration gradient induced by the slow-cooling method is clearly shown. (The numerical values $T_1 - T_2$ = 20°C, $x_1 - x_2$ = 0.03 and $V \sim 8 \times 16 \times 16$ mm^3 correspond roughly to the numerical example detailed in the description of fig. 3.)

clearly shows a spatial variation of the concentration between 0.002 and 0.006 mole mm^{-1} with superimposed periodic concentration fluctuations (i.e. the striations, considered in section 6). This gradient effect is also present in our crystals (see fig. 10). An ultrasonic method was employed to determine T_c (details are given in section 6). The concentration was determined from the known concentration dependence of T_c, and the gradient was found to be smaller than the literature value quoted above. However, a quantitative comparison is not possible because the position of the sample investigated within the crystal (i.e. the distance from the nucleation centre) was not given in the above-quoted papers.

In order to minimize the gradient effect, and to prepare samples of smallest inhomogeneity, optimum cuts are employed, as shown in fig. 5. In an idealized picture, a crystal grown at the bottom of the crucible consists of five growth sectors, the boundaries of which can usually be seen by the naked eye. Samples for physical measurements should be taken out of a single sector to avoid crossing the disturbed boundary regions. Within the sector, the sample is chosen as near as possible to the centre due to the smaller concentration gradient there (eq. (4)). The longest direction of the sample should be parallel to the equal-concentration planes, e.g. parallel to the grown faces, whereas the shortest direction of the sample should

when it is prepared by slow cooling from a solution. The spatial dependence of the concentration x within a crystal (see fig. 4) along the growth direction z for a small temperature interval is

$$x(z) = x_1 + 4(x_2 - x_1)z^3/V. \qquad (3)$$

The concentration gradient is then given by

$$\Delta x/\Delta z = 12(x_2 - x_1)z^2/V. \qquad (4)$$

As shown by an example in fig. 4, the concentration gradient is flat near the nucleation centre and becomes steeper in the last-grown part of the crystal; a general feature of mixed crystals grown by temperature variation.

The characterization of the KTa$_{1-x}$Nb$_x$O$_3$ crystals [12,47] grown by Bonner et al. [29,32]
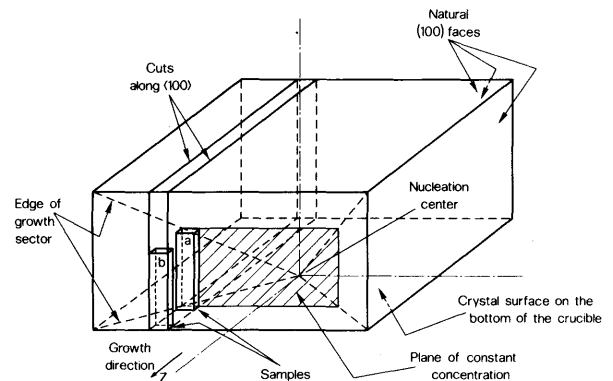

Fig. 5. Scheme of an as-grown crystal with its five natural faces and corresponding growth sectors. Optimum samples should be cut from single growth sectors. Sample (a) has a smaller $\Delta x/\Delta z$ gradient than sample (b).

be vertical to the faces, in the direction of the concentration gradient. All these considerations have been taken into account for the acoustic-resonance probes and for the samples used in the experiments described in sections 6 and 7.

5. Crystal-growth experiments

The KTa$_{1-x}$Nb$_x$O$_3$ growth experiments were performed in a commercial 12 kW chamber furnace [48]. Temperature control and programming were achieved by a central PID controller connected with an electronic ramp generator [49]. A flat temperature profile in the furnace chamber was obtained by two additional differential PID controllers and appropriate distribution of the power to the nine MoSi$_2$ heating elements. The general concepts of temperature control, furnaces, etc. have already been described [3c] so that only a few important details are discussed below.

In order to achieve a higher temperature sensitivity than the conventional Pt versus Pt–10% Rh thermocouple, thermopiles of the combination Pt–6% Rh versus Pt–30% Rh, with a high sensitivity above 800°C and a negligible sensitivity around room temperature, were employed [50]. The positions of the thermocouple junctions between the heating elements and the crucibles as well as the PID time constants were optimized so that a temperature control around 1400°C of 0.1°C was achieved (cf. fig. 7). A detailed description of the temperature-control system will be given elsewhere [51].

The furnace chamber (25 × 20 × 30 cm^3) is large enough to accommodate simultaneously from five to eight small crucibles of 50 or 180 ml and one larger platinum crucible on the ACRT apparatus. ACRT [4] is a stirring technique which allows homogenization of solutions in sealed crucibles. Nucleation control is achieved, and the maximum stable growth rate is increased [52]. Crucibles of special shapes [3f] as shown in fig. 6, with argon-arc-welded lids, and of 300 or 500 ml size were used in the present experiments. The dip in the centre of the bottom allows localized cooling and is thus a preferred site for nucleation. Short platinum tubes welded to the lid and to the bot-
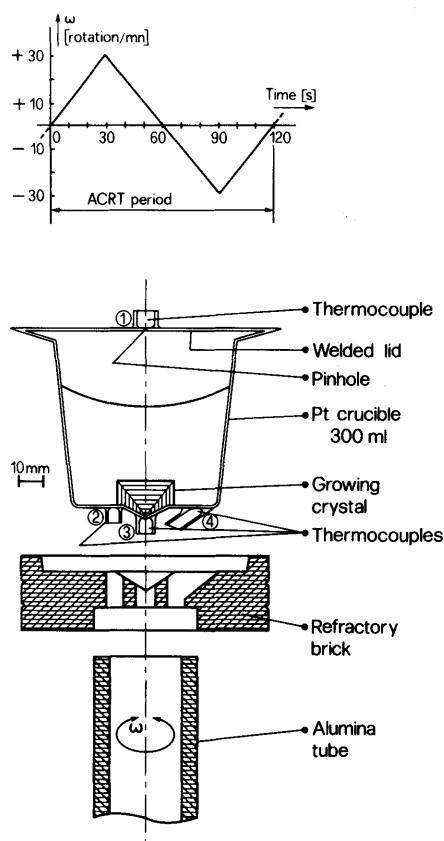

Fig. 6. Side view of a 300 ml crucible used in ACRT experiments. A typical ACRT period is also shown. For the thermocouple numbers, see also fig. 7.

tom of the crucible allow Pt–6% Rh versus Pt–30% Rh thermocouples to be partially embedded for local temperature measurements during the experiment; the connection copper wires below the furnace are long enough to permit periodic up- and de-winding during the ACRT action.

The steps of a typical growth experiment are schematically shown in fig. 7. During the first 20 h, the melt is homogenized at maximum ACRT rotation rates of 90 rpm and at a temperature about 50°C above the liquidus temperature. Then the temperature is lowered to a temperature T_0 about 5°C above the liquidus, and the cooling programme of −0.15°C/h is started. During the growth phase, maximum ACRT rotation rates of 30 or 60 rpm and periods of 60 and 120 s are used.
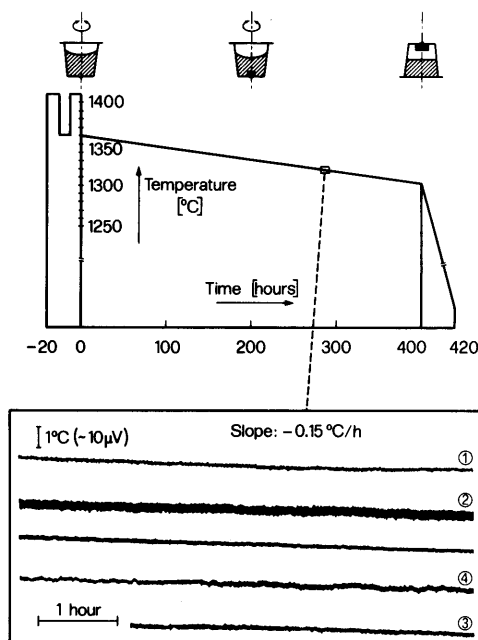
Fig. 7. Different steps of a growth experiment. A short interval during cooling is shown on a real temperature plot. The numbers correspond to the thermocouples of fig. 6. The unlabelled thermocouple was located at the back of the furnace.

When the final temperature T_2, around 1300°C, is reached the crucible is inverted to separate the grown crystals from the solution, cooled at a rate of 5°C/h to 900°C and then at 20°C/h to room temperature. The total experiment lasts about three weeks.

Preliminary experiments in the smaller crucibles, without ACRT, were made to evaluate the optimum growth conditions. The samples required for the quantum-limit investigations were cut from crystals grown in the large crucibles by using ACRT. Data of such ACRT experiments [53] are listed in table 3.

The liquidus temperature T_L and the effective nucleation temperature (e.g. the critical supersaturation) are not accurately known. This uncertainty may be due to the following:
(i) There is a difference of solidus and liquidus temperatures between the two published phase diagrams of the system $KTaO_3$–$KNbO_3$ [5,6] of 15 to 90°C. Our growth-experiment temperatures were adjusted at somewhat lower values than those of Reisman et al. [5]. At least partially, this is due to the unpredictable undercooling required for nucleation.

Table 3
Experimental parameters of several growth experiments and resulting crystals

Expt. No.	Crucible (ml)	x_{melt}	$KTaO_3$ (g)	$KNbO_3$ (g)	K_2CO_3 (g)	CO_2 in melt (g)	Observed loss (g)	Duration of experiment (h)
10	500	0.070	727.8	36.8	71.4	23	31	374
30	500	0.030	1000.0	20.9	144.0	46	46	430
45	500	0.030	1000.0	20.9	144.0	46	54	431
51	500	0.040	1000.0	27.9	133.8	46	53	393

[a] Temperature measurement at the top of the crucible. At the bottom, the temperature is about 10°C lower; with the used crucibles a gradient of 1°C/cm is thus observed.
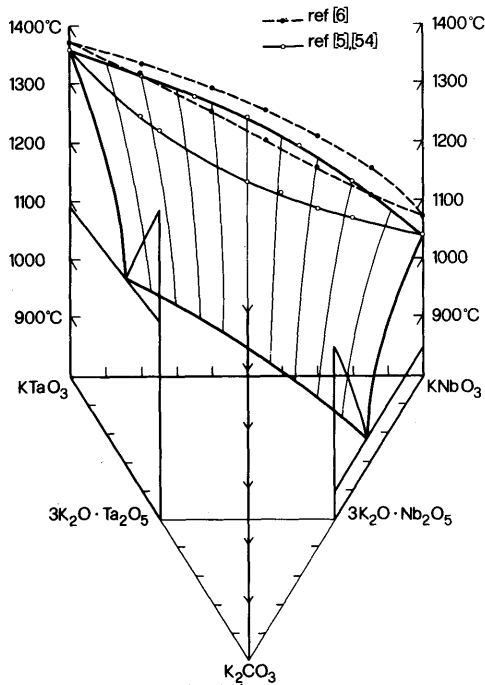[b] About 80% of the total crystal volume is inclusion free.

Fig. 8. Plots of the two published phase diagrams of $KTaO_3$–$KNbO_3$ solid solutions [5,6] together with parts of the diagrams for Ta_2O_5–K_2CO_3 and Nb_2O_5–K_2CO_3 [54]. A tentative diagram for $KTaO_3$–$KNbO_3$ with an excess of K_2CO_3 is also shown. An analog diagram has been given in an unpublished report by Rubin [40].

(ii) The K_2CO_3 excess reduces the liquidus temperature as was pointed out by Rubin [40]. This is illustrated in the tentative phase diagram of $KTaO_3$–$KNbO_3$–K_2CO_3 shown in fig. 8. Qualitatively, this diagram is supported by DTA measurements [35]. Thus, the temperature T_L should be reduced by about 50 to 100°C when working with 60 mole% K_2CO_3.

(iii) Other somewhat uncontrolled parameters are the gradual dissociation of K_2CO_3 leading to gaseous CO_2, and the evaporation of flux $K_3(Ta, Nb)O_4$ through the pinhole of the crucible lid. The total weight losses of typical experiments are included in table 3.

Despite these uncertainties, "reproducible" crystal-growth results (size, concentrations) were obtained when the experimental conditions were kept as identical as possible (see fig. 9).

6. Concentration measurements, striations

In the concentration range considered $(0 < x \leqslant 0.04)$, dielectric-constant measurements are not suitable to determine the ferroelectric transition temperature T_c because of the strong deviations

T_0 [a] (°C)	T_2 [a] (°C)	ACRT (rpm/s)	Number of crystals	Weight (g)	Size (mm³)	Inclusion [b] and strain-free part (mm³)	$x_{measured}$ (mean values)
1341	1295	30/60	5	115	Not well facetted	10×5×5	0.018±0.003
1354	1293	60/60	1	83	26×24×16	16×10×5	0.008±0.002
1353	1290	60/60	3	45	25×25×12	10×10×5	
				6	14×11× 5		
				6	14×10× 4		
1343	1288	60/60	4	114	35×30×18	10×10×5	
				34	22×22× 7		
				19	18×18× 9		
				15	16×13× 8		

Fig. 9. $KTa_{1-x}Nb_xO_3$ crystal grown by slow cooling of the melt. The data of the actual growth experiment are given in table 3 (see No. 45). Marker represents 25 mm.
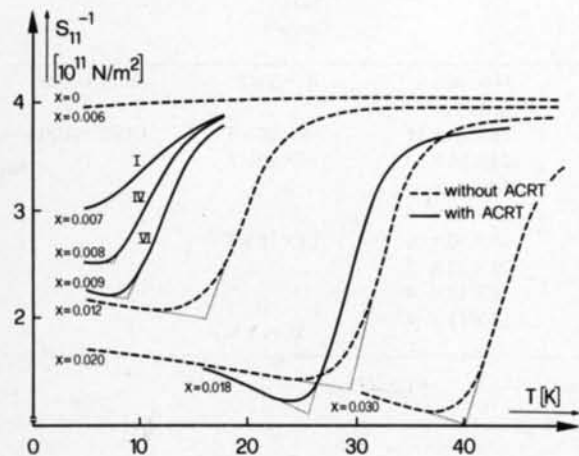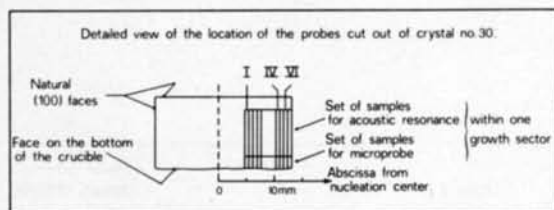
from Curie–Weiss behaviour in the quantum regime [27]. Therefore, acoustic resonance [24] was performed on samples cut out of the as-grown crystal according to the guidelines given in section 4. The samples are about $8 \times 1 \times 0.5$ mm^3 in size with edges along $\langle 100 \rangle$. Their largest faces are electroded to allow application of electric fields. Due to electromechanical coupling, a length-extensional vibration mode may be excited by a small AC field. If l and ρ denote the length of the sample and its density, respectively, then the mode frequency f is directly related to the inverse elastic

Fig. 10. Acoustic-resonance measurements: The resulting elastic compliance s_{11}^{-1} is plotted as a function of temperature. Each curve consists of about fifty data points. The dotted straight lines allow a graphical determination of T_c (corresponding to the temperature at the intersection point). Knowing T_c and the ferroelectric phase diagram (see fig. 1) one may label the curves with the corresponding concentration value. Samples I to VI are cut out of the same crystal, as shown in the upper part.

Table 4
Literature data on striations in $KTa_{1-x}Nb_xO_3$ crystals, with experimental methods used for detection

Refs.	Length scale (μm)	ΔT_c (°C)	Δx	Polarized light	Lattice parameter	X-ray topography	T_c measurements	Electrooptic effects	Electron microprobe	Etching
[29], [32]	Small regions	10	0.02	×						
[12]	1000 and smaller spacings	6	0.01	×	×					
[47]	50 and bands	1 and 6–18	0.002 and 0.01–0.03	×		×	×			×
[30]				×						
[55]		4.1	0.006	×				×		
[33]				×						
[34]				×			×			
[31]	5			×						
[56]	40			×						
[41]	25	18	0.03	×					×	
[40]				×						
Present work	1?	<1	<0.00025	×			×		×	×

compliance s_{11}^{-1} by $f = 1/(2l)\sqrt{s_{11}^{-1}/\rho}$. A characteristic "elastic step" occurs at the ferroelectric phase transition.

The experimental results are shown in fig. 10 together with the graphical determination of T_c. It should be noted that the elastic step is sharper in the case of ACRT-grown crystals, thus allowing more precise T_c measurements. The concentration values were obtained from the ferroelectric phase diagram (see fig. 1 and ref. [24]) and checked with electron-microprobe measurements. The samples labelled I to VI in fig. 10 were cut out of the same crystal (No. 30 in table 3): One clearly notices the concentration gradient along the growth direction. Acoustic resonance is thus a sensitive method to achieve a global determination of the mean concentration in samples near the quantum limit.

So far, only macroscopic aspects of the concentration variation have been discussed by considering continuous variations of x on a spatial scale comparable to the size of the grown crystals (i.e. about 10 mm). In KTa$_{1-x}$Nb$_x$O$_3$, as example for most solid solutions, there are generally periodic or non-periodic concentration fluctuations on a much smaller (but still macroscopic) scale: These *striations* have seriously limited the technological applications of KTa$_{1-x}$Nb$_x$O$_3$. In table 4, the literature data on striations in KTa$_{1-x}$Nb$_x$O$_3$ solid solutions are compiled together with the applied experimental methods and with the data from the present work.

Usually, striations are attributed to cyclic variations of the concentration x, thus a periodically banded structure appears with the bands parallel to the crystal faces within the respective growth sector. These striations are induced during the growth process by growth-rate fluctuations caused by the corresponding temperature fluctuations (rarely by fluctuations of other parameters like hydrodynamics or pressure). The fluctuating temperatures arise either from temperature control of the furnace, or from oscillating convection. Whiffin [41] pointed out that the observed inhomogeneity $\Delta x = 0.03$ in his TSSG-grown KTa$_{0.64}$Nb$_{0.36}$O$_3$ crystal would imply temperature oscillations of $\pm 7.5°C$ while he measured in the melt $\pm 0.4°C$. This discrepancy may possibly be explained by significant temperature gradients in his growth

system leading to strong surface-tension-gradient-driven convection (Marangoni convection) in addition to buoyancy-driven convection. Local temperature fluctuations may thus have been generated near the growing crystal. They were possibly not detected by the temperature measurements, the temperature sensor being located relatively far away from the crystal and deep in the melt.

Striations of crystals, grown immersed in high-temperature solutions stirred by ACRT, can be caused (i) by temperature oscillations, (ii) by hydrodynamic oscillations, and (iii) by growth-rate fluctuations due to growth instability.

(i) Temperature oscillations at the growing-crystal interface can be induced (a) by the temperature control of the furnace, (b) by periodically changing forced convection like ACRT, (c) by natural buoyancy-driven convection, and (d) by Marangoni convection. The latter two effects can be ruled out in our case because the temperature gradient outside the crucible is only $1°C/cm$, the solution is homogenized by forced convection, and since both platinum and the melt have high thermal conductivities thus minimizing buoyancy-driven convection as well as surface-tension gradients leading to the Marangoni convection. A quantitative estimate is not possible because the temperature dependence of the surface tension of KTaO$_3$:K$_3$TaO$_4$ melts is not known. Natural and Marangoni convection are present in other crystal-growth techniques with inherently large temperature gradients (for example TSSG, Verneuil and zone melting [57]).

The precision of the temperature-control system is $0.1°C$ as measured at various positions in the furnace (see fig. 7). This corresponds to concentration changes $\Delta x = 0.00025$; in practice, Δx will be much smaller due to the large thermal masses and conductivities of the crucible and the (stirred) melt, and due to the sluggish response of the crystallization processes to temperature changes. As indicated in fig. 7, the largest temperature fluctuations at the crucible wall (thermocouple No. 2) are induced by ACRT: they are of the order of $\pm 0.25°C$. The temperature difference between top and bottom of the crucible is about $10°C$, and despite the stirring effect of ACRT there remains a temperature oscillation due to alternating accelera-

tion and deceleration of the crucible rotation. These temperature oscillations could possibly be reduced by minimizing the temperature gradient and by further optimization of the ACRT parameters. The temperature change of 0.5°C would correspond to a maximum concentration change of $\Delta x = 0.00125$, which however is reduced by the damping effects of the melt and of the growth kinetics. The periodicity of the expected ACRT striations would range between 0.3 and 1.2 μm according to the mean growth rate of 10 to 40 nm s^{-1}.

(ii) Hydrodynamic oscillations by natural convection and by Marangoni convection are small due to the small temperature gradients on the one hand, and to the stirring effect of ACRT on the other. Thus, only ACRT could have an effect on the hydrodynamics and the diffusion boundary layers around the growing crystal. During the acceleration and deceleration phase, the boundary layers have the same magnitude, with minor deviations caused by the changing flow direction and the local asymmetry around the growing crystal. A change of the diffusion boundary-layer thickness occurs only during switching from acceleration to deceleration and vice versa. Since this transient time (of the order of a fraction of a second) is short compared to the ACRT period, and since the growth rate reacts slowly to boundary-layer changes, the effect on the composition change will be small, and anyhow on a scale ($\sim$ 10 nm) which cannot be detected by conventional characterization methods. For crystal growth from solutions, in the case of growth-rate limitation by volume diffusion, hydrodynamic fluctuations themselves do not have a significant effect on crystal homogeneity as discussed by Scheel and Schulz-Dubois [57]. Striations, in this case, are induced only by temperature fluctuations in connection with hydrodynamic oscillations.

(iii) If the growth rate reaches or surpasses the maximum stable value (where inclusions and other forms of instability like hopper growth or dendrites occur [52]), an oscillatory behaviour of the growth rate may be observed as described by Landau [58]. Depending on the degree of instability, the oscillatory growth rates may cause striations or inclusion bands. For growth of high-quality crystals, supersaturation should be adjusted for growth in the stable regime so that instability-induced inhomogeneities cannot occur.

In our ACRT experiments, crystals were obtained with large defect-free regions ($8 \times 4 \times 4$ mm^3), where on the one hand, no striations could be detected by microprobe measurements, and on the other, only faint bands could sometimes be seen by polarization microscopy.

The electron-microprobe experiments [59] were performed with an electron beam of 15 kV and a current of 150 nA, with KTaO$_3$ and KNbO$_3$ single crystals as standards. Several areas of 6.7×6.7 μm^2 were investigated, and due to the low Nb concentrations, long counting times (40 s) were applied. Measurements along the growth direction on probes I to VII (see fig. 10) revealed that, in a given sample, the Nb concentration remained constant within 0.25% of the measured value (i.e. for sample I: $x = 0.00700 \pm 0.00002$). It should be noted, however, that these data have been obtained in close vicinity to the ultimate detection limit of the microprobe.

From these experiments, it appears to us that it is not meaningful to conclude on the existence or non-existence of striations in the presently analysed crystals. What we may state is that no striations with large ($\geqslant$ 10 μm) spacings have been observed. Nevertheless, striations with smaller spacings in the 1 μm range may still occur. They possibly correspond to the faint bands that appeared weakly contrasted between crossed polarizers. A tentative explanation would be to ascribe them to ACRT-induced temperature fluctuations.

7. Strain and dislocations

In the case of transparent crystals (such as KTa$_{1-x}$Nb$_x$O$_3$), bulk defects are readily observed by optical microscopy. In this section, the major bulk defects encountered in our crystals will be described according to the strain patterns generated and the dislocations revealed by etching.

Fig. 11 shows several typical strain patterns displaying the following defects. Inclusions are observed in the zones where the growth rate exceeded the stability limit. This is always the case at the beginning of growth in a slow-cooling experi-
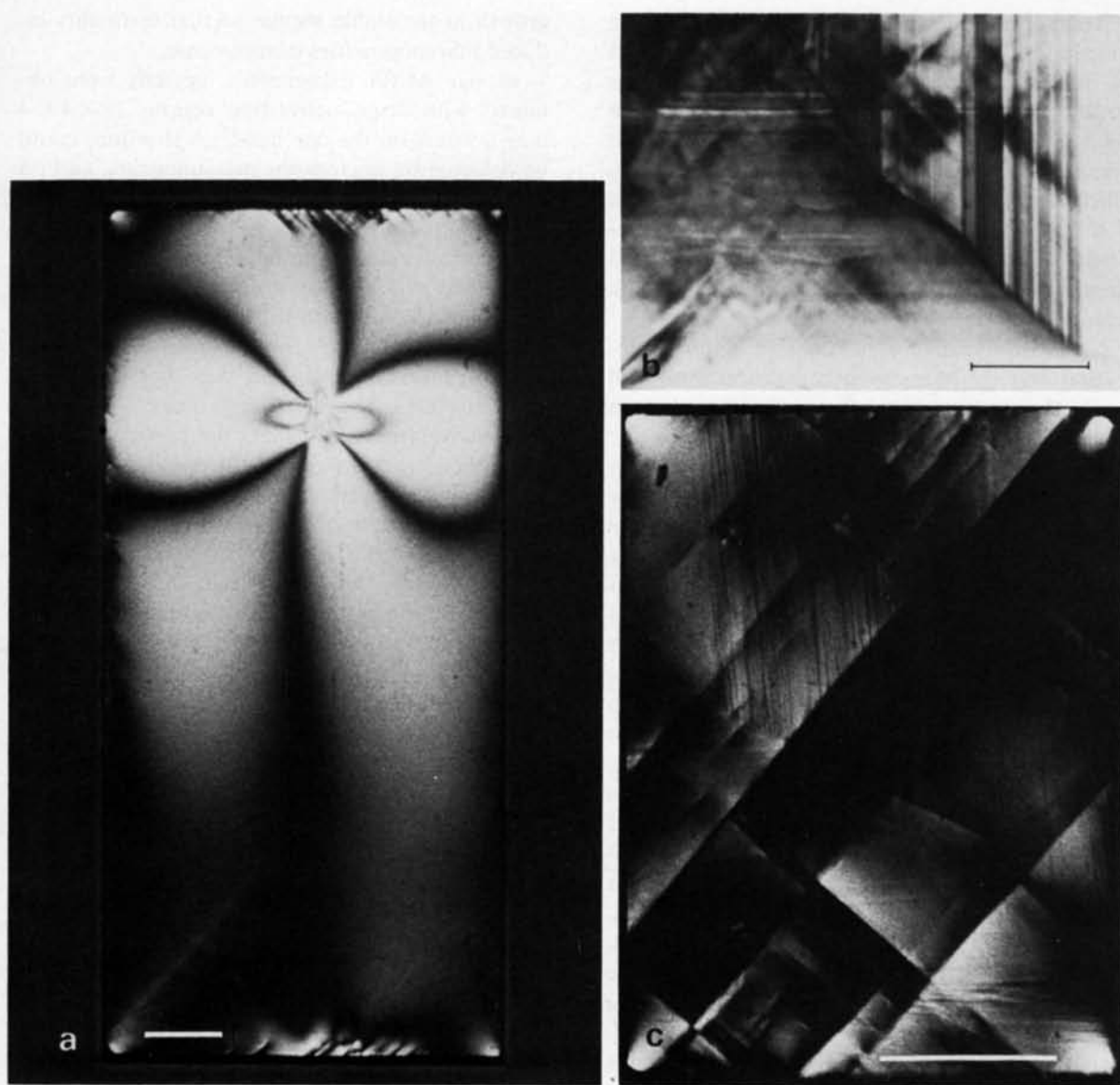
Fig. 11. Strain patterns viewed between crossed polarizers of (a) an inclusion, (b) a growth-sector boundary where, to enhance the contrast, a heavily striated crystal grown without ACRT was chosen, (c) cross-hatch. Markers represent 1 mm.

ment when an "infinitely" large growth rate is achieved due to the singularity of the surface/volume fraction and due to the large initial supersaturation. The picture shown in fig. 11a was obtained for an inclusion located at a growth-sector boundary such as in fig. 11b. The latter is a planar defect corresponding to the intersection of two growth sectors with perpendicular growth directions (see also section 4). In fig. 11c, an example is given of the so-called "cross-hatch" structure which consists of a network of sharp $\langle 110 \rangle$ lines possibly typical of $KTa_{1-x}Nb_xO_3$ crystals [12,31]. This structure is very intense for crystals having a large contact area with the crucible, and it is
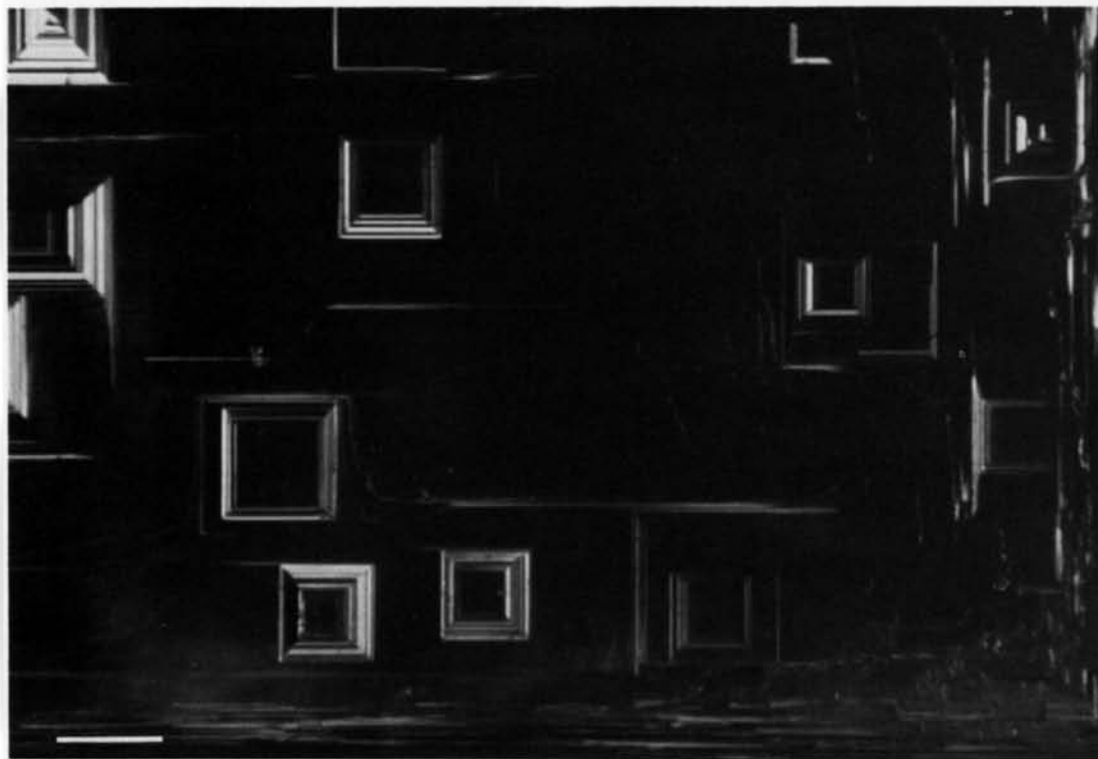
Fig. 12. Etch pits on a (100) face. Marker represents 100 μm.

therefore tempting to attribute it to microtwins induced by the aftergrowth cooling.

In order to have an estimate of the dislocation density in our crystals, an etch-pit technique was employed. Immersing a sample in 50 wt% KOH and 50 wt% NaOH at 200°C during 10 min resulted in the structure shown in fig. 12. Five different samples were investigated and it was seen that the mean etch-pit density ranges between 10^4 and 10^2 cm^{-2}, the latter value corresponding to the ACRT-grown samples. Unfortunately, there are too few data reported in the literature (a density of 5×10^2 cm^{-2} is indicated [47] for crystals grown by Bonner et al. [29,32]) to make a sensitive correlation between the dislocation density and growth parameters such as temperature gradient and growth rate. Nevertheless, it may be expected that the dislocation density in crystals grown immersed in solutions is somewhat lower than in TSSG-grown crystals due to the smaller temperature gradient at the liquid–solid interface [60].

Acknowledgements

References

[1] J.E. Geusic, S.K. Kurtz, L.G. Van Uitert and S.H. Wemple, Appl. Phys. Letters 4 (1964) 141;
F.S. Chen, J.E. Geusic, S.K. Kurtz, J.G. Skinner and S.H. Wemple, J. Appl. Phys. 37 (1966) 388.

[2] U.T. Höchli, Ferroelectrics 35 (1981) 17.

[3] D. Elwell and H.J. Scheel, Crystal Growth from High-Temperature Solutions (Academic Press, London, 1975) p. 294 (a), p. 386 (b), p. 334 (c), p. 343 (d), p. 264 (e), p. 368 (f), p. 263 (g).

[4] H.J. Scheel and E.O. Schulz-DuBois, J. Crystal Growth 8 (1971) 304;
H.J. Scheel, J. Crystal Growth 13/14 (1972) 560; see also ref. [3b].

[5] A. Reisman, S. Triebwasser and F. Holtzberg, J. Am. Chem. Soc. 77 (1955) 4228.

[6] P.D. Garn and S.S. Flaschen, Anal. Chem. 29 (1957) 275.

[7] A. Reisman and E. Banks, J. Am. Chem. Soc. 80 (1958) 1877.

[8] S. Wemple, MIT Tech. Rept. No. 425 (1964).

[9] P. Vousden, Acta Cryst. 4 (1951) 373.

[10] D.G. Demurov and Yu.N. Venevtsev, Soviet Phys.-Solid State 13 (1971) 553.

[11] G.A. Samara and B. Morosin, Phys. Rev. B8 (1973) 1256.

[12] R.L. Barns, Mater. Res. Bull. 2 (1967) 273.

[13] A.W. Hewat, K.D. Rouse and G. Zaccai, Ferroelectrics 4 (1972) 153.

[14] G. Shirane, R. Newnham and R. Pepinsky, Phys. Rev. 96 (1954) 581.

[15] A.W. Hewat, J. Phys. C6 (1973) 2559.

[16] H. Uwe and T. Sakudo, J. Phys. Soc. Japan 38 (1975) 183.

[17] E. Wiesendanger, Ferroelectrics 6 (1974) 263.

[18] A.C. Nunes, J.D. Axe and G. Shirane, Ferroelectrics 2 (1971) 291.

[19] S. Triebwasser, Phys. Rev. 114 (1959) 63.

[20] L.T. Todd, Masters Thesis MIT (1969), unpublished.

[21] C.H. Perry, R.R. Hayes and N.E. Tornberg, in: Molecular Spectroscopy of Dense Phases, Eds. M. Grosman, S.G. Elkomoss and J. Ringeisen (Elsevier, Amsterdam, 1976) p. 267.

[22] L.A. Boatner, U.T. Höchli and H.E. Weibel, Helv. Phys. Acta 50 (1977) 620.

[23] S.K. Kurtz, Bell System Tech. J. 45 (1966) 1209.

[24] U.T. Höchli, L.A. Boatner and H.E. Weibel, Phys. Rev. Letters 32 (1977) 1158.

[25] T. Schneider, H. Beck and E. Stoll, Phys. Rev. B13 (1976) 1123.

[26] R. Oppermann and H. Thomas, Z. Physik B22 (1975) 387.

[27] D. Rytz, U.T. Höchli and H. Bilz, Phys. Rev. B22 (1980) 359.

[28] P.W. Whipps, J. Crystal Growth 12 (1972) 120.

[29] W.A. Bonner, E.F. Dearborn and L.G. Van Uitert, Am. Ceram. Soc. Bull. 44 (1965) 9.

[30] W.R. Wilcox and L.D. Fullmer, J. Am. Ceram. Soc. 49 (1966) 415.

[31] V.G. Hill and R.I. Harker, Tech. Rept. AFML-TR-66-343 (1966);
V.G. Hill, L.L.Y. Chang and R.I. Harker, J. Am. Ceram. Soc. 51 (1968) 723.

[32] W.A. Bonner, E.F. Dearborn and L.G. Van Uitert, in: Crystal Growth, Ed. H.S. Peiser (Pergamon, Oxford, 1967) p. 437.

[33] D.J. Marshall and R.A. Laudise, in: Crystal Growth, Ed. H.S. Peiser (Pergamon, Oxford, 1967) p. 557.

[34] A.L. Gentile and F.H. Andres, Mater. Res. Bull. 2 (1967) 853.

[35] V.D. Salnikov and V.I. Shelankin, Tr. Vses. Nauchn.-Issled. Inst. Khim. Reakt. Osobo Chist. Khim. Vechestv. 30 (1967) 415.

[36] T. Fukuda, H. Hirano and S. Koide, J. Phys. Soc. Japan 24 (1968) 430.

[37] A.F. Dugan and W.M. Doyle, IEEE Trans. Electron Devices ED-16 (1969) 522.

[38] V. Belruss, J. Kalnajs, A. Linz and R.C. Folweiler, Mater. Res. Bull. 6 (1971) 899.

[39] W.B. Yelon, W. Cochran, G. Shirane and A. Linz, Ferroelectrics 2 (1971) 261.

[40] J.A. Rubin, Ceradyne, Inc., Report AD-764 902 (1973).

[41] P.A.C. Whiffin, Mullard Research Lab. Report No. 2848 (1973);
P.A.C. Whiffin and J.C. Brice, J. Crystal Growth 23 (1974) 25.

[42] L.A. Boatner, A.H. Kayal and U.T. Höchli, Helv. Phys. Acta 50 (1977) 167.

[43] A.M. De Goër, B. Salce and L.A. Boatner, in: Phonon Scattering in Condensed Matter, Ed. H.J. Marris (Plenum, New York, 1980) p. 243.

[44] D.M. Hannon, Phys. Rev. 164 (1967) 366.

[45] J.M. Courdille, J. Dumas, S. Ziolkiewicz and J. Joffrin, J. Physique 38 (1977) 1519.

[46] B. Okai, M. Tsukioka and T. Fujita, Japan. J. Appl. Phys. 19 (1980) L248.

[47] S.A. Levy and R. Gashler, Mater. Res. Bull. 3 (1968) 417.

[48] Superkanthal® furnace of Käsermann and Spérisen S.A., Bienne, Switzerland.

[49] Eurotherm, Glattbrugg, Zurich, Switzerland.

[50] H.J. Scheel and C.H. West, J. Phys. E6 (1973) 1178; see also ref. [3d].

[51] P. Dill, H.J. Scheel and D. Widmer, in preparation.

[52] H.J. Scheel and D. Elwell, J. Crystal Growth 12 (1972) 153; see also refs. [3e,3g].

[53] Grade 1 chemicals of Johnson Matthey were used.

[54] A. Reisman, F. Holtzberg, M. Berkenblit and M. Berry, J. Am. Chem. Soc. 78 (1956) 4517;
A. Reisman and F. Holtzberg, J. Am. Chem. Soc. 77 (1955) 2117.

[55] H. Fay, Mater. Res. Bull. 2 (1967) 499.

[56] C. Forno and O.C. Jones, Nature 230 (1971) 375.

[57] H.J. Scheel and E.O. Schulz-DuBois, in: Convective Transport and Instability Phenomena, Eds. J. Zierep and H. Oertel (Braun, Karlsruhe, 1982).

[58] A.I. Landau, Phys. Metals Metallog. 6 (1958) 148.

[59] ARL electron microprobe of the Centre de Microanalyse par Sonde Electronique, Université de Lausanne.

[60] H.J. Scheel, Progr. Crystal Growth Characterization, to be published.